Low-Field Mode Transitions in a Spiral-Antenna Helicon Thruster

IEPC-2019-848

Presented at the 36th International Electric Propulsion Conference
University of Vienna, Austria
September 15-20, 2019

Justin M. Little*
University of Washington, Seattle, WA, 98105, USA

The low-magnetic-field mode transition in a spiral-antenna helicon thruster is examined using experiment and theory. Helicon plasma sustainment in low-magnetic fields (< 100 G) is desirable for electric propulsion because it could provide improved power coupling and mass utilization to a variety of thruster concepts without the use of heavy electromagnets. However, operation in the low-field helicon mode balances reduced magnet mass with increased wall losses – a tradeoff that largely depends on the maximum magnetic field that can sustain the mode. To understand the nature of the mode transition, an analytical model is derived that couples 0D mass and power conservation equations with the m=0 wave dispersion relation. The model predicts that the low-field mode transition occurs when the wave phase velocity exceeds the point where sufficient wave energy is absorbed by the plasma electrons via Landau damping. From this result, a general scaling law for the mode transition field strength is derived in terms of thruster power, mass flow rate, geometry, and propellant properties. Finally, the predicted scaling is validated using experimental data from a spiral antenna helicon thruster.

I. Introduction

Radio frequency (RF) plasma sources have been proposed for electric propulsion applications due to their ability to efficiently ionize propellant gas without the use of lifetime-limiting, plasma-facing electrodes. RF plasmas play a key role in a variety of thruster architectures currently in development, including RF gridded-ion thrusters,[1–3] helicon plasma thrusters,[4] two-stage Hall thrusters,[5] and VASMIR.[6] One characteristic of RF plasma sources that is particularly important to a number of thruster concepts is the mode by which power from the RF antenna couples to the propellant plasma. Capacitive (E), inductive (H), and helicon (W) modes have been observed and studied for different source geometries,[7–9] antenna types,[8,10–12] pressures,[13] and power levels.[14] Of these, the helicon mode produces the highest power transfer efficiencies and ionization fractions due to the ability of helicon waves to propagate and deposit power into regions of the plasma beyond the plasma skin depth. For this reason, it is typically desired that RF plasma sources for electric propulsion operate in the helicon mode for effective utilization of onboard power and propellant mass.

Helicons refer to a specific class of right-handed polarized (RHP) electromagnetic waves that propagate in a magnetized plasma at wave frequencies between the ion and electron cyclotron frequencies ($\omega_{ci} \ll \omega \ll \omega_{ce}$).[15] For helicon-sustained plasma sources, wave energy is deposited into plasma electrons by virtue of collisional and collisionless damping mechanisms.[16] Starting with the cold-plasma dispersion relation (CPDR),[17] it can be shown that helicon wave propagation requires the presence of a background magnetic field, B_0, which is linearly related to the plasma density, $n_e \sim B_0$, for a fixed wavelength (often determined by the antenna geometry). Constraints associated with wave propagation manifest in E-H-W mode transitions, marked by sudden changes in plasma density following small changes in either pressure, power, or magnetic field strength. A direct E-W mode transition has been observed in a number of experiments operating at low magnetic fields (< 50 Gauss).[18–23] Despite being particularly attractive for electric propulsion applications

*Assistant Professor, William E. Boeing Department of Aeronautics & Astronautics, littlej7@uw.edu

due to the favorable scaling of magnet mass and power with decreased field strength, the low-field helicon mode has received much less attention that its high-field counterpart. Early work by Chen et al identified the low-field helicon mode and characterized its behavior for uniform magnetic fields[18] . Chen later showed that the low-field density peak results from wave reflection at the plasma axial boundary.[19] Seminal work by Lafleur, Charles, and Boswell characterized the behavior,[21] power balance,[22] ion beam formation,[20] and wave propagation[21] for a low-field mode in the presence of diverging magnetic fields. Notably, most experimental studies have used finite length antennas that produce an m=1 helicon mode. Chen observed that the low-field mode is more pronounced for an m=0 loop antenna.[19] Although not identified as such, results from Steven's et al using a spiral antenna also suggest the existence of a low-field m=0 helicon mode.[11]

In this paper, we use experimental observations to characterize the behavior and scaling of the low-field mode transitions for a spiral antenna plasma source and converging magnetic field topology. Combining helicon wave theory with a global plasma model for mass and energy conservation, the following questions are examined: *For the m=0 mode, what is the effect of removing the constraint on the axial wavelength of the helicon wave? How does wave energy couple into the plasma?* Finally, the results of this analysis are used to examine the scaling of m=0 low-field helicon modes for electric propulsion applications.

II. Experimental Setup

Data was obtained from the magnetic nozzle experiment at Princeton University.[24,25] The plasma source (PS) consists of a 7.5 cm inner diameter, 30.5 cm long tube of borosillicate glass mounted concentrically inside two electromagnetic coils (Fig. 1). The tube is wrapped with grounded copper mesh to prevent stray RF fields outside of the device.[26] A two-turn spiral antenna is positioned within the glass tube behind a Macor backplate, which also serves to isolate the antenna from plasma. Working gas is fed through the center of the Macor backplate using an alumina tube. The RF signal is produced by an Agilent 8648B signal generator. An ENI 2100L pre-amplifier steps the signal up to approximately 20 W, which is fed into an Alpha 9500 linear amplifier capable of producing 1.5 kW. An Alpha 4520 digital wattmeter is used to monitor the standing-wave ratio (SWR) and determine the power delivered to the matching network/antenna (P_D). Power is transferred to the antenna via an L-type impedance matching network that is mounted inside of the vacuum chamber and mechanically isolated from the thrust stand. The matching network was designed such that the antenna leads are mounted on two copper rail electrodes aligned parallel to the axis of the device. The combination of this rail system combined and movable backplate allows adjustment of the axial position of the antenna and gas injection location, and therefore the channel length, within a 13 cm range.

Two electromagnetic coils are placed near the exit of the plasma source to form a magnetic nozzle.[27] The electromagnets were made by wrapping 144 turns (12 × 12) of AWG 10 square, copper magnet wire around an aluminum mandrel. The mean current radius was measured to be $r_c = 7.51$ cm, which corresponds closely to the physical radius of the center of the copper windings. The magnets are powered using an Amrel SPS32 DC switching power supply, and are each capable of handling up to 50 A of current. The magnets were

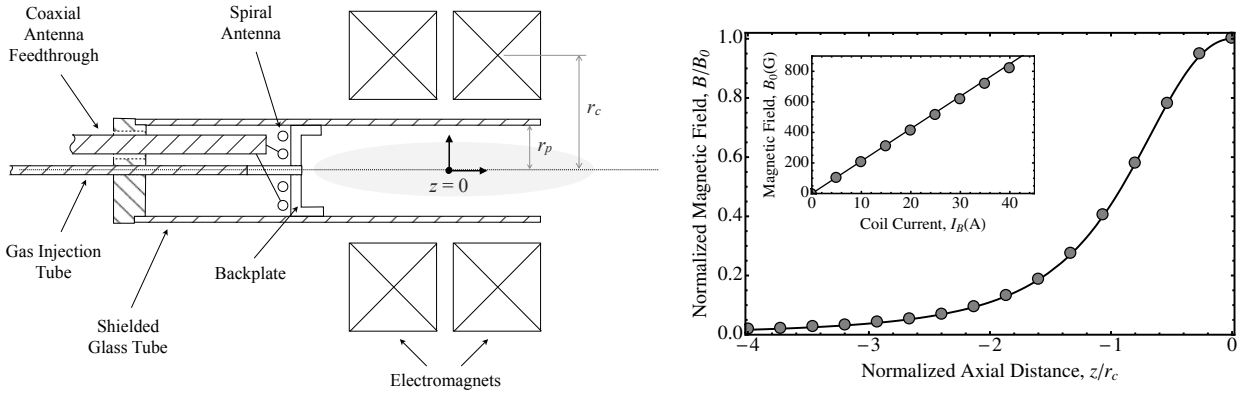

Figure 1. Schematic of the spiral antenna helicon thruster (left) and dependence of the magnetic field strength on distance from the magnetic nozzle center (right) and magnet current (right inset)

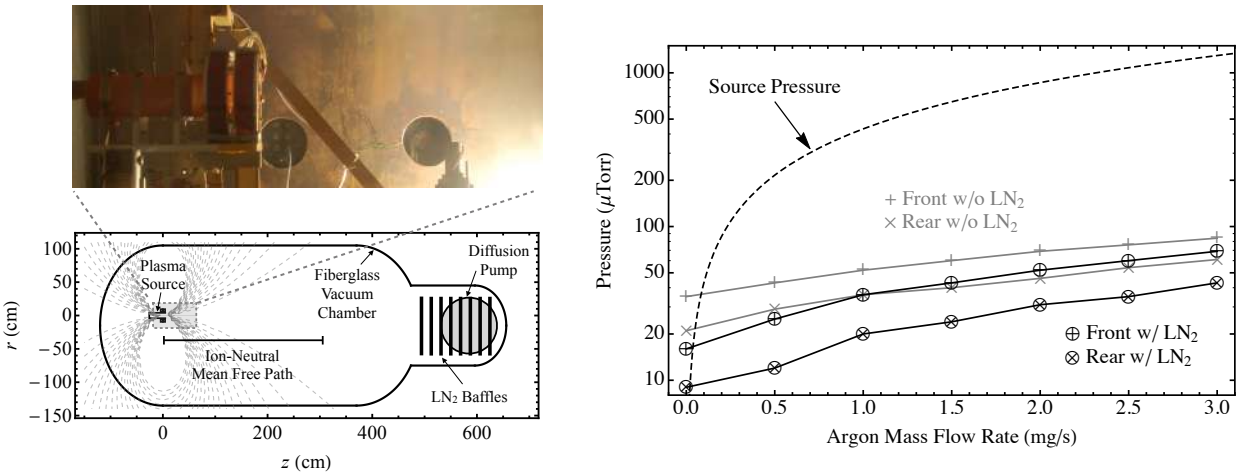

Figure 2. Photograph of the spiral antenna helicon thruster installed in the EPPDyL orange tank (upper left) along with relative dimensions of the thruster and chamber (lower left). Measurements of the steady state pressure versus Ar mass flow rate for the experimental measurements contained in this paper (right).

designed such that they can move independently with respect to each other and the glass tube, thus allowing control over the physical and magnetic geometries of the PS. A single configuration is used throughout the duration of this experiment whereby the magnets are connected rigidly together with an axial separation of 4.5 cm between their effective centers. Gaussmeter measurements of the relative magnetic field strength along the nozzle axis are shown in Fig. 1. The magnitude of the maximum magnetic field as a function of the coil current, I_B, is also shown in the inset. The solid black lines in Fig. 1 result from approximating the two magnets as single loops of current with radius r_c. Continuing with this approximation, the surfaces of constant magnetic flux are shown in Fig. 2 as dashed lines.

The plasma flow exhausts into EPPDyL's Large Dielectric Pulsed Propulsion (LDPP) vacuum chamber (Fig. 2). The cylindrical chamber is made out of fiberglass and measures 8 ft. in diameter and 25 ft. in length. The chamber is evacuated using two mechanical Stokes roughing pumps, a roots blower, and a 48 inch diameter CVC diffusion pump rated at 95,000 l/s of pumping capacity (N_2). The facility is also equipped with liquid nitrogen (LN_2) baffles to further reduce the pressure and halt contamination due to back streaming diffusion and roughing pump oil. Pressure is measured using a Varian ConvectTorr vacuum gauge and two Varian 525 cold cathode gauges connected to a Varian L8350 multi-gauge controller. The vacuum system has a minimum base pressure of 0.2 μTorr, however, vacuum leaks restricted the base pressure of the present experiments to 20 μTorr without the LN_2 baffles and 0.9 μTorr with the LN_2 baffles. We show in Fig. 2 how the steady-state operating pressure of the tank varied as a function of the Ar mass flow rate into the PS. These measurements were made using cold cathode gauges mounted in the front (near the PS) and rear (near the diffusion pump) of the chamber. As expected, the operating pressure increases with the mass flow rate, and is generally higher towards the front of the tank. We also show in Fig. 2 the expected gas pressure within the PS. With the exception of very low mass flow rates, we see that the PS pressure is an order of magnitude larger than the chamber pressure.

III. Observation of the LFMT

We found the PS to operate in three distinct modes (see Fig. 3) depending on the mass flow rate, applied magnetic field strength, injection location, and RF power. We refer to these modes according to the established modes in RF plasmas:[16] the capacitive mode (E), inductive mode (H) and helicon wave mode (W). The characteristics of each mode are consistent with those observed in the literature, however, we did not make wave measurements to confirm wave propagation within the helicon mode.[8]

The discharge was most commonly ignited in the E mode, which was distinguished by a faint glow with electron temperatures and ion densities on the order $T_e \sim 10$ eV and $n_i \sim 10^{16} - 10^{17}$ m^{-3}. For fixed P_D and $\dot{m}$, as we *decreased* the magnetic field below a certain threshold the plasma would jump into either the

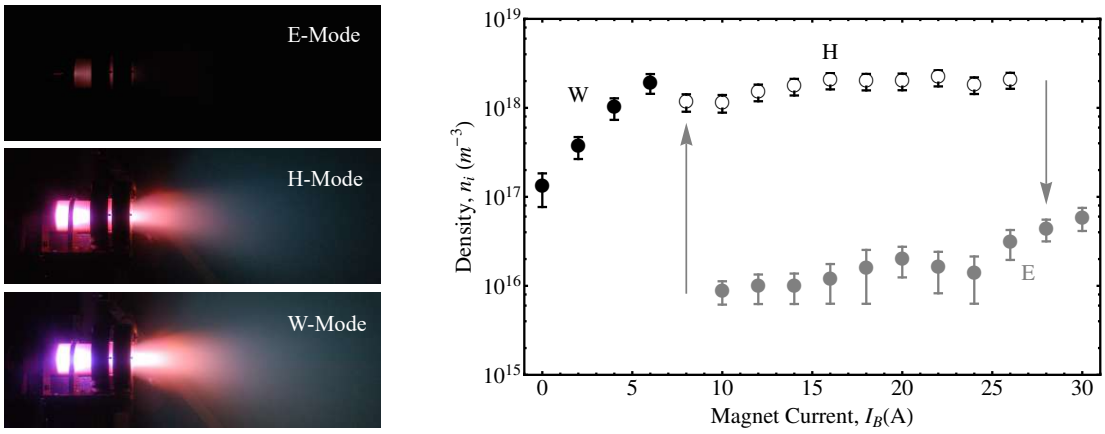

Figure 3. Photographs of the thruster operating in the three observed modes (left). Measurements of electron density versus magnetic field strength exhibit jumps at the different mode transitions (right).

H or W mode, leading to an impedance mismatch that had to be corrected using the tuning capacitors. Further decreases in field strength initiated the H-W mode transition, which required additional tuning of the matching capacitors. The plasma was observed to be much brighter in the W mode and demonstrated the "blue core" characteristic of Helicon plasmas reported in the literature.[28] The temperature and density of the W mode were measured to be $T_e \sim 5$ eV and $n_i \sim 10^{18} - 10^{19}$ m^{-3}, respectively. The H mode was slightly less bright than the W mode and did not possess a "blue core." We observed T_e to be comparable between the W and H modes, while n_e showed a slight decrease upon transitioning from the W to H mode. We note that the density in the W mode appears lower than that of the H mode at low magnetic fields in Fig. **??** due to diffusion of the plasma to the PS walls prior to reaching the LP (located at $z = 0$). This behavior highlights the importance of understanding the low-field W-mode transition. Specifically, the increased performance of the low-field W mode is only beneficial so long as the mode can be sustained at magnetic field strengths large enough to prevent substantial plasma wall losses.

The high ionization fraction and power coupling efficiency make the W mode most relevant to electric propulsion applications. For this reason, we seek a better understanding of the conditions required to sustain the W mode at low magnetic fields. While in the W mode, the plasma responded to increasing magnetic field strength in one of two ways depending on the mass flow rate. For low mass flow rates (generally < 1.0 mg/s of Ar), the plasma was observed to transition directly from the W to E modes. At higher mass flow rates, a W-H-E mode transition was observed (as shown in Fig. 3). Irrespective of the channel length (L_{bp}), mass flow rate ($\dot{m}$), and RF power (P), the plasma inevitably transitioned out of the W mode at a particular magnetic field strength, which we will refer to as the mode transition field strength, B_0^*. Fig. 4 shows the dependence of B_0^* on experimental parameters L_{bp}, $\dot{m}$, and P. From Fig. 4 the following conclusions can be made about the low-field W mode transition (LFMT):

- B_0^* increases with L_{bp}, $\dot{m}$, and P.
- B_0^* is more sensitive to changes in P than $\dot{m}$
- The sensitivity of B_0^* to changes in $\dot{m}$ and P increases with L_{bp}.

Furthermore, for large L_{bp}, B_0^* reaches values an order of magnitude larger than previously observed in the literature. Finally, we note that the absence of data points at low values of L_{bp} and $\dot{m}$ indicates that a low-field W mode was not observed at these conditions.

IV. LFMT Theoretical Model

We now turn to theory to better understand the nature and scaling of the observed LFMT. Mode transitions in RF plasmas can be modeled analytically by combining an equation for RF power absorption with plasma mass and power conservation equations. To this end, we follow the approach of Chabert

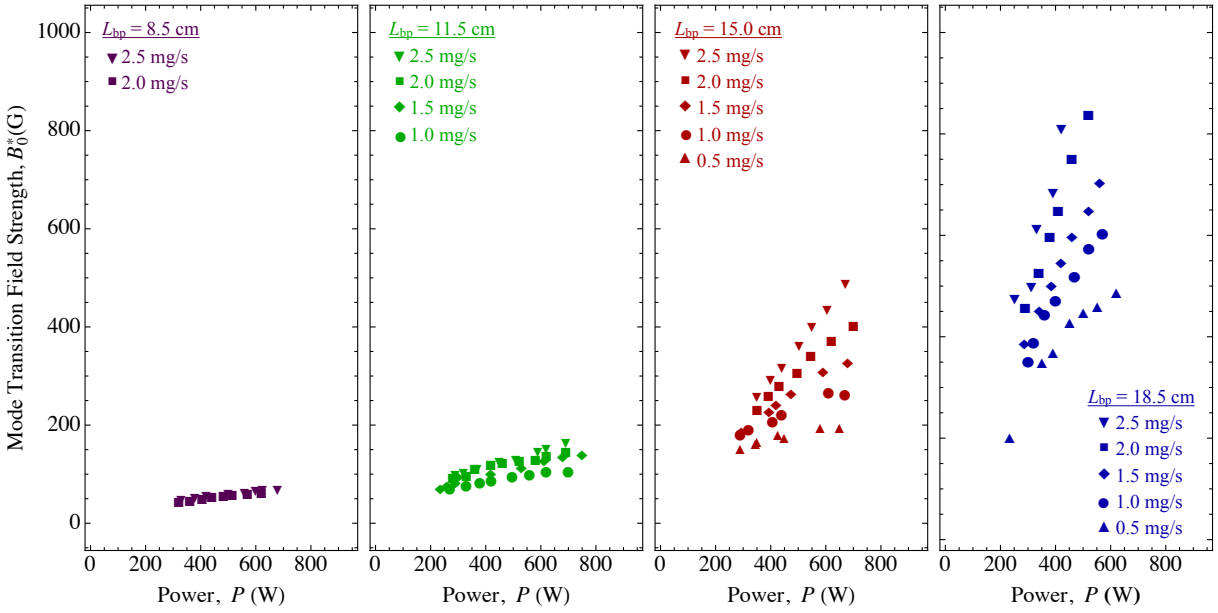

Figure 4. Magnetic field strength at which either a W-H or W-E mode transition occurred. Measurements are shown for different power levels (P), mass flow rates ($\dot{m}$), and backplate locations (L_{bp}).

and Braithwaite in which RF power absorption is determined from the helicon wave dispersion relation for a cold uniform plasma.[16] Combined with a global (0D) model for the plasma discharge, the mode transition can be examined by considering the balance of power within the plasma. While the use of the uniform dispersion relation and 0D-model neglect geometric effects associated with plasma and magnetic field anisotropies, it ultimately enables us to derive a simple scaling law for the LFMT as a function of the plasma density, temperature, and radius, which we then relate to the experimental parameters via the global model. Geometric effects are then included *a posteriori* using the magnetic field profile.

A. Helicon Wave Propagation and Absorption

Helicons are one of many types of plasma waves that can propagate in a cold uniform plasma within a background magnetic field. Their dependence on the properties of the plasma and background field can be described using the cold plasma dispersion relation (CPDR).[17] For an effective collision frequency, ν_{eff}, the CPDR may be written in the following form[16]

$$kk_z = \frac{\omega\omega_{\mathrm{pe}}^2}{c^2\omega_{\mathrm{ce}}}\left(1 - \frac{i\nu_{\mathrm{eff}}k}{\omega_{\mathrm{ce}}k_z}\right), \tag{1}$$

which is valid for $\omega_{\mathrm{ci}} \ll \omega \ll \omega_{\mathrm{ce}}$ and $\nu_{\mathrm{eff}} \ll \omega_{\mathrm{ce}}\cos\theta$. Here, ω, ω_{ci}, ω_{ce}, and ω_{pe} represent the wave, ion cyclotron, electron cyclotron, and plasma frequency, respectively. The wavenumber is denoted k and its axial component k_z. For the $m = 0$ mode, the radial wavenumber is constrained to $k_r = a_1/r_p$, where r_p is the plasma radius and $a_1 \approx 3.83$. The speed of light is represented by c.

The mechanism by which helicon wave energy is absorbed by the plasma is presently a topic of debate. In most helicon plasma sources, electron collisions with neutral particles and ions are too infrequent to explain experimentally observed absorption rates. A number of alternative mechanisms have been proposed, including kinetic effects such as Landau damping[29] and wave-particle trapping,[30] or transformation of the helicon wave (via mode coupling[31] or parametric decay[32]) into wave modes (e.g. ion acoustic or Trivelpiece-Gould waves) that are more strongly damped at the collision frequencies common to these devices. Here, we adopt the absorption model of Chen whereby wave energy is absorbed by the electron population via electron-ion collisions and Landau damping.[29] The effective collision frequency may be written as

$$\nu_{\mathrm{eff}} = \nu_{\mathrm{ei}} + \nu_w, \tag{2}$$

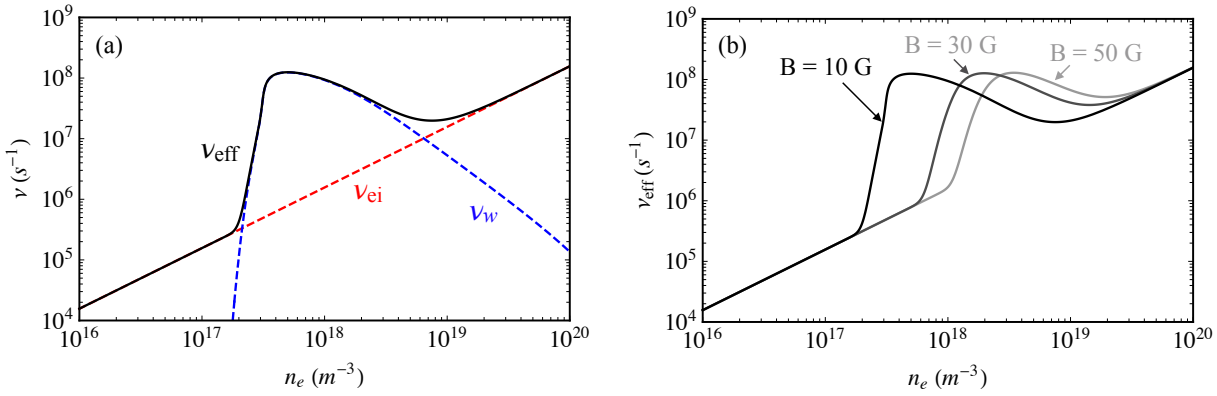

Figure 5. (a) Effective collision frequency for wave absorption ($\nu_{\rm eff}$) along with the electron-ion collision frequency ($\nu_{\rm ei}$) and equivalent collision frequency for Landau damping (ν_w). (b) The peak in $\nu_{\rm eff}$ shifts towards higher densities as the magnetic field increases. Argon gas is assumed along with the following: $T_{\rm ev} = 7$ eV, $\omega/(2\pi) = 13.56$ MHz, and $r_p = 3.75$ cm.

with

$$\nu_w = 2\sqrt{\pi}\xi^3\omega\exp\left(-\xi^2\right) \tag{3}$$

being the equivalent collision frequency associated with collisionless Landau damping of the wave. Here, $\xi = \sqrt{2}v_\phi/v_e$, where v_ϕ and $v_e = \sqrt{eT_{\rm ev}/m_e}$ are the wave phase velocity and electron thermal velocity, respectively. The electron-ion frequency (in units of Hz) is given by

$$\nu_{\rm ei} \approx 2.9 \times 10^{-11} n_e T_{\rm ev}^{-3/2}. \tag{4}$$

Here, $T_{\rm ev}$ represents the electron temperature in units of eV.

A plot of the effective collision frequency is shown as a function of electron density in Fig. 5(a) for parameters representative of the experimental conditions within the PS. It is clear from this figure that the effective wave collision frequency is over two orders of magnitude larger than the electron-ion collision frequency for $n_e \sim 10^{17} - 10^{18}$ m^{-3}. Fig. 5(b) shows that, for fixed conditions, as the magnetic field increases the peak in ν_w shifts to higher densities. This can be explained by noting that the maximum in ν_w occurs at a fixed value of $\xi^* = \sqrt{3/2}$. Because $v_\phi \sim B/n_e$, and v_e is independent of both B and n_e, the maximum in ν_w occurs at a fixed ratio of B/n_e for a given T_e.

B. Theoretical Model for the LFMT

We consider for now a cylindrically symmetric plasma source with a uniform magnetic field along the z-direction. The characteristic absorption length of the helicon wave along the axis of the plasma source, α_z, is given by the imaginary component of the axial wavenumber,

$$\alpha_z = -\frac{1}{\mathrm{Im}\left(k_z\right)}. \tag{5}$$

Using this expression along with Eqs. (1)-(4), the power asborbed by a plasma of length L via helicon wave damping is given by

$$P_{\rm abs}^W = \eta_c P_{\rm rf}\left[1 - \exp\left(-\frac{2L}{\alpha_z}\right)\right], \tag{6}$$

where $P_{\rm rf}$ is the RF power and η_c the antenna-plasma coupling efficiency.

Mode transitions from the W to E mode can be analyzed by introducing a phenomenological model for power absorption via capacitive coupling,[16]

$$P_{\rm abs}^E = \frac{c_E}{n_e}. \tag{7}$$

Here, c_E is a constant whose value can be chosen to yield densities in the range of experimentally observed values. The total power absorbed by the plasma is then taken as

$$P_{\text{abs}} = P_{\text{abs}}^W + P_{\text{abs}}^E. \tag{8}$$

Note that the introduction of Eq. (7) merely provides a second stable equilibrium solution, and does not influence the transition away from the W mode.

Mode transitions occur when conditions within the plasma change such that the absorbed power can no longer balance the power lost by the plasma. Power is typically lost through a variety of physical processes, including particle diffusion and convection, inelastic collisions, and radiation. We adopt the following simplified model for these loses

$$P_{\text{loss}} = n_e u_i \pi r_p^2 \left(\epsilon_{\text{ke}} + \epsilon_w + \epsilon'_{\text{ion}}\right), \tag{9}$$

where $u_i = \sqrt{\gamma e T_{\text{ev}}/m_i}$ is the ion acoustic speed and γ the electron polytropic index. The energies ϵ_{ke}, ϵ_w, and ϵ'_{ion} represent the kinetic energy, effective energy lost to the wall, and effective ionization energy per ion leaving the device. We also assume plasma leaving the source accelerates through a magnetic nozzle to a final exhaust velocity, $u_{\text{ex}} = g_u u_i$, with $g_u = \sqrt{(\gamma+1)/(\gamma-1)}$.[33] The kinetic energy per ion is then given by

$$\epsilon_{\text{ke}} = \frac{1}{2} m_i \left(g_u u_i\right)^2. \tag{10}$$

For simplicity, we assume the radial walls of the chamber are fully shielded and that the power lost to the rear wall of the thruster approximately equals the kinetic power of the exhaust, $\epsilon_w \approx \epsilon_{\text{ke}}$. Finally, to account for radiative losses, the effective ionization energy is taken as twice the ionization energy of the gas, $\epsilon'_{\text{ion}} \approx c_{\text{ion}} \epsilon_{\text{ion}}$ with $c_{\text{ion}} = 2$.

The absorbed power and power loss curves are shown as a function of density in Fig. 6(a) for three magnetic field strengths. Note that stable equilibrium requires that both $P_{\text{abs}} = P_{\text{loss}}$ and $dP_{\text{abs}}/dn_e < dP_{\text{loss}}/dn_e$. For low magnetic fields, three equilibrium solutions exist, two of which are stable. The stable high density solution occurs when power losses are balanced by helicon wave absorption, thus representing the W mode. Alternatively, the stable low density solution represents the E mode. As the magnetic field increases, the plateau in P_{abs} shifts to higher n_e. In this region $P_{\text{abs}} \approx P_{\text{abs}}^W$, therefore the shift in P_{abs} is primarily the consequence of the shift in ν_w, as shown in Fig. 5(b). Eventually, the ν_w-curve shifts to densities that are too high to be sustained for the given loss curve, leaving only one stable solution – the E mode. Physically this occurs because the phase velocity of the wave increases along with the magnetic field. Eventually the phase velocity reaches a point where there is an insufficient quantity of electrons within the portion of phase space in which wave energy is absorbed via Landau damping. Further increases in magnetic field (and therefore density) beyond this point require the loss curve be shifted to the right by either decreasing the effective energy lost per ion or increasing the power density.

Fig. 6(b) shows the density as a function of magnetic field strength for both the W and E modes for the same case shown in Fig. 6(a). Similar to what we observe experimentally, the plasma can exist in either the E or W mode at low magnetic fields. Increasing the magnetic field within the W mode eventually leads to a W-E mode transition, as described above. The E-mode persists with additional increases to the magnetic field. Finally, the W mode can be recovered by decreasing the magnetic field to sufficiently low values to induce an E-W mode transition. Although not immediately apparent, the decreased density with magnetic field strength observed experimentally in Fig. 2 is also consistent with our LFMT theoretical model. This is because the power lost to the walls would in reality increase significantly as $B \to 0$. As a result, ϵ_w increases as B decreases, thus shifting the loss curve to lower densities. However, we note that Eq. (1) is not valid as $B \to 0$ and a different form of the CPDR is required to properly describe this limit.

C. General Scaling of the LFMT

Scaling of the LFMT can be examined by noting that the plateau in the absorbed power curve scales with the peak of the equivalent wave collision frequency curve. Our general approach is to use an approximation of the CPDR to derive an analytical expression for the magnetic field strength that maximizes ν_w for a given n_e and T_{ev}. To reasonable accuracy, the field strength associated with the W-E mode transition can then be taken as some constant times the ν_w-maximizing field strength.

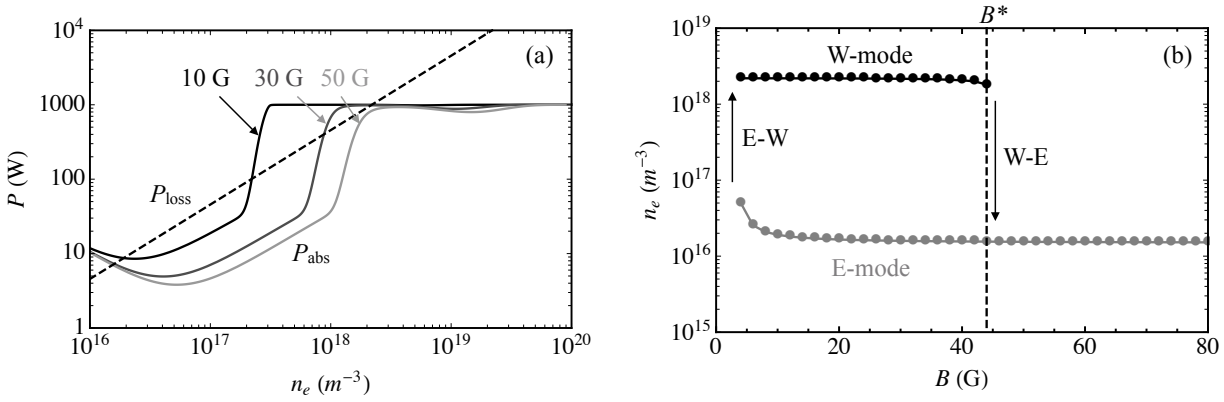

Figure 6. (a) Curves for the absorbed power ($P_{\rm abs}$) and lost power ($P_{\rm loss}$) demonstrate the W-E mode transition as the magnetic field strength is increased from 10 G to 50 G. (b) The density versus magnetic field curves show a region of low magnetic field where the two modes can both exist in stable equilibrium. The transition between the two modes at the ends of this region are marked by arrows. Argon gas is assumed along with the following: $T_{\rm ev} = 7$ eV, $\omega/(2\pi) = 13.56$ MHz, and $r_p = 3.75$ cm.

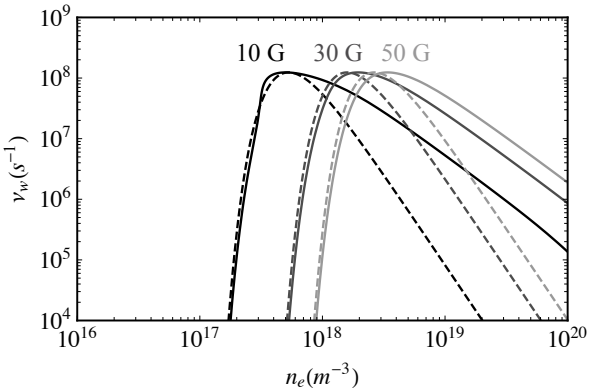

Figure 7. Curves for the equivalent wave collision frequency (ν_w) as a function of electron density (n_e). Solid and dashed lines represent ν_w calculated using the full and approximate expressions for k_z, respectively. Argon gas is assumed along with the following: $T_{\rm ev} = 7$ eV, $\omega/(2\pi) = 13.56$ MHz, and $r_p = 3.75$ cm.

Solving for the value of ξ at which $d\nu_w/d\xi = 0$ yields

$$\xi_m \equiv \frac{\sqrt{2}\omega}{k_{z,m} v_e} = \sqrt{\frac{3}{2}}, \tag{11}$$

where $k_{z,m}$ is the axial wavenumber associated with the maximum in ν_w. $\mathrm{Re}(k) \gg \mathrm{Im}(k)$ when $k_r \gg k_z$ and $\nu_{\rm eff} \ll \omega_{\rm ce}$. In this limit, Eq. (1) may be approximated as

$$k_{z,m} \approx \frac{\omega \omega_{\rm pe}^2}{c^2 \omega_{{\rm ce},m} k_r}. \tag{12}$$

Fig. 7 compares ν_w calculated using both the dispersion relation given in Eq. (1) and the approximate form shown in Eq. (12). It is clear from this figure that Eq. (12) provides a good approximation for both the region of increasing ν_w with n_e, and the location and value of the maximum of ν_w.

The combination of Eqs. (11) and (12) yields an expression for the value of the electron cyclotron frequency that maximizes ν_w,

$$\omega_{{\rm ce},m} = \frac{\sqrt{2}\omega_{\rm pe}^2 v_e}{c^2 k_r}. \tag{13}$$

Eq. (13) describes how the ν_w-maximizing magnetic field scales with the plasma density, temperature, and plasma radius. This equation can be re-written as

$$B_m = b_0 r_p n_e T_{\mathrm{ev}}^{1/2}, \tag{14}$$

where

$$b_0 = \frac{\sqrt{3} e^{3/2}}{2 a_1 \epsilon_0 c^2 m_e^{1/2}} \tag{15}$$

depends only on fundamental constants.

Finally, noting that the mode transition roughly coincides with a shift in the plateau of P_{abs} to the right of P_{loss}, the LFMT field strength approximately scales according to

$$B^* \approx \chi B_m = \chi b_0 r_p n_e T_{\mathrm{ev}}^{1/2}. \tag{16}$$

where χ is a constant that depends on the general shape of the ν_w curve. We find that a value of $\chi \approx 2$ comes to within $< 30\%$ of the exact numerical solution over a large range of relevant conditions. Eq. (17) represents a general equation for the magnetic field strength at which an $m = 0$ plasma transitions away from the low-field W-mode.

D. LFMT Scaling with Thruster Parameters

We seek to use Eq. (17) along with a global model for the plasma discharge to derive scaling laws that describe how the LFMT varies with thruster parameters such as the mass flow rate, input power, and geometry. The mass flow rate of ions in a quasineutral, uniform plasma flow is given by $\dot{m}_i = m_i n_e u_i \pi r_p^2$. Eq. (17) can then be written as

$$B^* = \frac{\chi b_1 \dot{m}_i}{r_p \sqrt{\gamma m_i}}, \tag{17}$$

where

$$b_1 = \frac{b_0}{\pi \sqrt{e}} \tag{18}$$

also depends only on fundamental constants.

Assuming $P_{\mathrm{abs}} \approx \eta_c P_{\mathrm{RF}}$ just prior to the LMFT (i.e. the power curves intersect near the plateau in P_{abs}), the power balance equation can be written in terms of the ion mass flow rate as

$$\eta_c P_{\mathrm{RF}} = \frac{\dot{m}_i}{m_i} \left(\epsilon_{\mathrm{ke}} + \epsilon_w + \epsilon'_{\mathrm{ion}} \right). \tag{19}$$

Solving for $\dot{m}$ and inserting into Eq. (18) yields

$$B^* = \frac{\chi b_1 \eta_c P_{\mathrm{RF}} \sqrt{m_i/\gamma}}{r_p \left(\epsilon_{\mathrm{ke}} + \epsilon_w + \epsilon'_{\mathrm{ion}} \right)}, \tag{20}$$

Both the kinetic energy per particle and wall loss energy scale linearly with T_e. Making the simplifying assumptions that $\epsilon'_{\mathrm{ion}} \ll \epsilon_{\mathrm{ke}} + \epsilon_w$ and $\epsilon_{\mathrm{ke}} \approx \epsilon_w$, Eq. (21) simplifies to

$$B^* = \frac{\chi b_1 \eta_c P_{\mathrm{RF}}}{2 r_p \mu(\gamma) e T_{\mathrm{ev}} \sqrt{\gamma m_i}} \tag{21}$$

where

$$\mu(\gamma) \equiv \frac{\gamma}{2} \left(\frac{\gamma + 1}{\gamma - 1} \right) = \frac{\gamma g_u^2}{2} \tag{22}$$

again results from ion acceleration through the magnetic nozzle at the exit of the plasma source. Eq. (22) describes the LMFT field strength in terms of the input power, electron temperature, species properties, and fundamental constants.

The electron temperature of helicon plasma sources generally increase with r_p and inversely with $\dot{m}$,[22] and typically falls in the range $T_{\mathrm{ev}} \in [4, 8]$ eV.[34] A relationship between T_e, $\dot{m}$, and r_p can be derived from mass conservation. The neutral and ion mass continuity equations combine into the following form

$$\dot{m}_i = \dot{m} \left(1 - e^{-\Lambda} \right) \approx \dot{m} \Lambda, \tag{23}$$

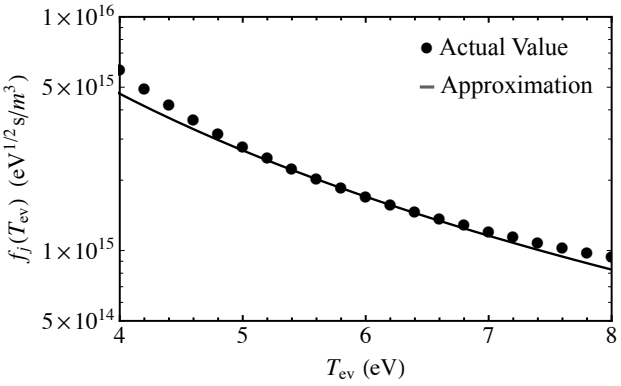

Figure 8. Actual value of the ionization function $f_j(T_{\rm eV})$ compared to the approximate form, $f_j(T_{\rm eV}) \approx c_j T_{\rm eV}^n$. Here, $c_j = 1.5 \times 10^{17}$ and $n = 2.5$.

where $\Lambda \equiv L/\lambda_{\rm ion}$ is the ratio of the plasma source length, L, to the mean free path for electron impact ionization, $\lambda_{\rm ion}$. The approximation on the right-hand side of Eq. (24) is valid for $\Lambda \ll 1$. Λ can be written in terms of the species-dependent ionization reaction rate, $R_{\rm ion}$, and neutral velocity, u_n, as

$$\Lambda = \frac{n_e R_{ion} L}{u_n}. \tag{24}$$

Algebraic manipulation of the approximate form of Eq. (24) and insertion of the equation for $\dot{m}_i$ for a uniform plasma flow yields the following transcendental equation describing the scaling T_e as a function of $\dot{m}$, species properties, and fundamental constants:

$$f_j\left(T_{\rm ev}\right) \equiv \frac{\sqrt{T_{\rm ev}}}{R_{\rm ion}\left(T_{\rm ev}\right)} = \frac{b_1 \dot{m} L}{b_0 \sqrt{\gamma m_i} u_n r_p^2}. \tag{25}$$

Finally, we make the approximation, $f_j(T_{\rm ev}) \approx c_j T_{\rm eV}^n$, where c_j is a species dependent constant and n represents a scaling parameter. A comparison between the actual value of f_j and the approximate form is shown in Fig. 7 for argon gas. It is apparent from this figure that, for the value $n = 2.5$, the approximation to f_j provides reasonable accuracy within the range of temperatures frequently observed in helicon sources. With this established, we invert the approximate equation for f_j to arrive at

$$T_{\rm ev} \approx \left(\frac{b_0 c_j u_n r_p^2 \sqrt{m_i/\gamma}}{b_1 \dot{m} L} \right)^{1/n}, \tag{26}$$

which describes the general scaling of the electron temperature with the mass flow rate into the thruster. Notably, Eq. (27) correctly predicts T_e to increase as r_p increases and $\dot{m}$ decreases.

Substitution of Eq. (27) into Eq. (22) yields the following general expression for the LMFT magnetic field strength as a function of the thruster geometry, operating parameters, and propellant species properties:

$$B^* = C_1 \frac{P_{\rm RF}}{r_p \sqrt{m_i}} \left(\frac{\dot{m} L}{c_j r_p^2} \right)^{1/n} \tag{27}$$

Here, we have combined all other constants into C_1. Eq. (28) is general in the sense that it describes how the LMFT field strength scales with thruster power and mass flowrate for a given geometry, constrained by the requirement that the electron temperature does not go outside the range associated with the values of c_j and n. However, extension of the scaling law to new gas species and electron temperature regimes simply requires one to recalculate the values of c_j and n.

We return to the experimental data to determine how well Eq. (28) predicts the scaling of the LMFT. We plot in Fig. 9 the measured LMFT field strength versus three different quantities. First, plotting B^* as

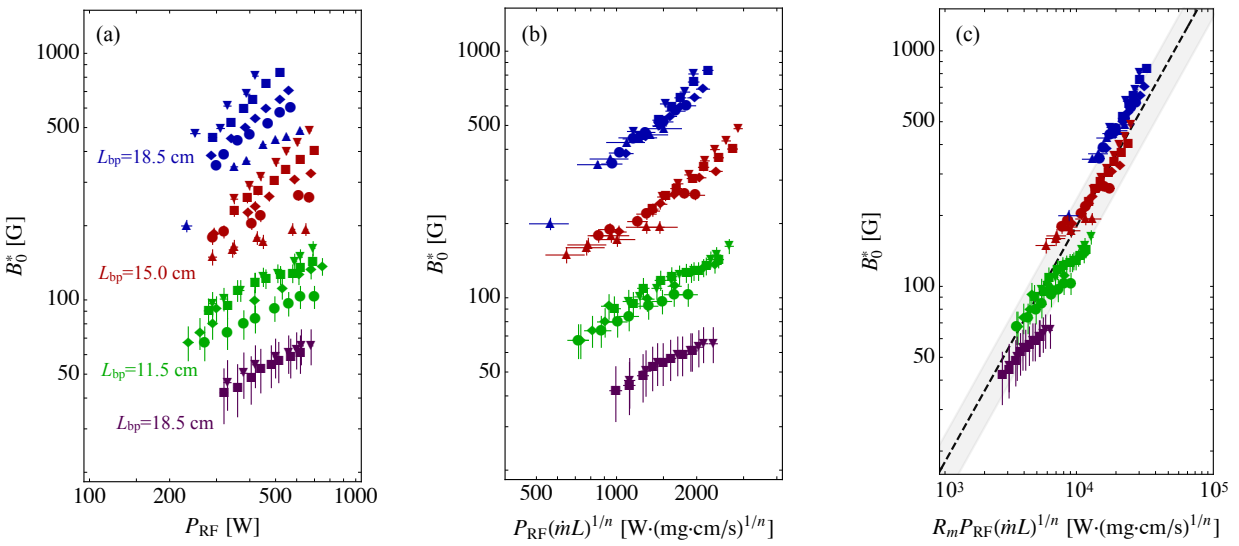

Figure 9. Dependence of the low-field mode transition field strength (B_0^*) on: (a) the delivered RF power (P_{RF}); (b) the quantity $P_{RF}(\dot{m}L)^{1/n}$; and (c) the quantity $R_m P_{RF}(\dot{m}L)^{1/n}$. Data points correspond to the legends shown in Fig. 3. The dashed line in (c) represents the scaling predicted from Eq. (28) with a correction for the diverging magnetic field topology.

a function of P_{RF} [Fig. (9)] shows that, although B^* can be seen to generally increase with P_{RF}, no clear trend emerges from the data. Adding the additional dependence of B^* on the quantity $(\dot{m}L)^{1/n}$ collapses the experimental data into four distinct lines, one for each value of L. Additional analysis shows that these lines follow the linear scaling predicted from Eq. (28).

The clustering of data for different L can be explained by accounting for the diverging magnetic field topology of the experiment. Eq. (28) was derived for a uniform magnetic field. In the experiment, however, the magnetic field strength at the center of the magnets is larger than at the antenna by the quantity $R_m = B_0/B(-L_{bp})$, where $B(z)$ is shown in Fig. (1). Correcting for the magnetic field, our theoretical model predicts that the LMFT field strength at the center of the magnets scales as $B_0^* = R_m B^*$, where B^* is defined in Eq. (28). Implementing this correction, Fig. (9) shows that the experimental data for the four values of L_{bp} collapse onto a single line. Here, the dashed line represents the predicted scaling from Eq. (17). The shaded area shows the region of 30% uncertainty in the slope that is attributed to variations in the parameter χ. We therefore find that the observed scaling is consistent with the theoretical model for the LMFT, which provides evidence that the mode transition occurs when the phase velocity of the wave increases to the point where wave absorption via Landau damping cannot sustain the discharge.

References

[1]Groh, K. and Loebt, H., "State-of-the-art of radio-frequency ion thrusters," *Journal of Propulsion and Power*, Vol. 7, No. 4, 1991, pp. 573–579.

[2]Chabert, P., Arancibia Monreal, J., Bredin, J., Popelier, L., and Aanesland, A., "Global model of a gridded-ion thruster powered by a radiofrequency inductive coil," *Physics of Plasmas*, Vol. 19, No. 7, 2012, pp. 073512.

[3]Goebel, D. M., "Analytical discharge model for RF ion thrusters," *IEEE transactions on plasma science*, Vol. 36, No. 5, 2008, pp. 2111–2121.

[4]Takahashi, K., "Helicon-type radiofrequency plasma thrusters and magnetic plasma nozzles," *Reviews of Modern Plasma Physics*, Vol. 3, No. 1, 2019, pp. 3.

[5]Shabshelowitz, A., Gallimore, A. D., and Peterson, P. Y., "Performance of a helicon Hall thruster operating with Xenon, Argon, and Nitrogen," *Journal of Propulsion and Power*, Vol. 30, No. 3, 2014, pp. 664–671.

[6]Bering, E., Chang-Diaz, F., Squire, J., Brukardt, M., Glover, T., Bengtson, R., Jacobson, V., McCaskill, G., and Cassady, L., "Electromagnetic ion cyclotron resonance heating in the VASIMR," *Advances in Space Research*, Vol. 42, No. 1, 2008, pp. 192–205.

[7]Loewenhardt, P., Blackwell, B., Boswell, R., Conway, G., and Hamberger, S., "Plasma production in a toroidal heliac by helicon waves," *Physical review letters*, Vol. 67, No. 20, 1991, pp. 2792.

[8]Ellingboe, A. and Boswell, R., "Capacitive, inductive and helicon-wave modes of operation of a helicon plasma source," *Physics of Plasmas*, Vol. 3, No. 7, 1996, pp. 2797–2804.

[9]Virko, V., Kirichenko, G., and Shamrai, K., "Geometrical resonances of helicon waves in an axially bounded plasma," *Plasma Sources Science and Technology*, Vol. 11, No. 1, 2002, pp. 10.

[10]Sudit, I. D. and Chen, F. F., "Discharge equilibrium of a helicon plasma," *Plasma Sources Science and Technology*, Vol. 5, No. 1, 1996, pp. 43.

[11]Stevens, J., Sowa, M., and Cecchi, J., "Helicon plasma source excited by a flat spiral coil," *Journal of Vacuum Science & Technology A: Vacuum, Surfaces, and Films*, Vol. 13, No. 5, 1995, pp. 2476–2482.

[12]Shinohara, S., Hada, T., Motomura, T., Tanaka, K., Tanikawa, T., Toki, K., Tanaka, Y., and Shamrai, K. P., "Development of high-density helicon plasma sources and their applications," *Physics of Plasmas*, Vol. 16, No. 5, 2009, pp. 057104.

[13]Corr, C. and Boswell, R., "High-beta plasma effects in a low-pressure helicon plasma," *Physics of Plasmas*, Vol. 14, No. 12, 2007, pp. 122503.

[14]Winglee, R., Ziemba, T., Giersch, L., Prager, J., Carscadden, J., and Roberson, B., "Simulation and laboratory validation of magnetic nozzle effects for the high power helicon thruster," *Physics of Plasmas*, Vol. 14, No. 6, 2007, pp. 063501.

[15]Klozenberg, J., McNamara, B., and Thonemann, P., "The dispersion and attenuation of helicon waves in a uniform cylindrical plasma," *Journal of Fluid Mechanics*, Vol. 21, No. 3, 1965, pp. 545–563.

[16]Chabert, P. and Braithwaite, N., *Physics of radio-frequency plasmas*, Cambridge University Press, 2011.

[17]Stix, T. H., *Waves in plasmas*, Springer Science & Business Media, 1992.

[18]Chen, F. F., Jiang, X., Evans, J., Tynan, G., and Arnush, D., "Low-field helicon discharges," *Plasma Physics and Controlled Fusion*, Vol. 39, No. 5A, 1997, pp. A411.

[19]Chen, F. F., "The low-field density peak in helicon discharges," *Physics of Plasmas*, Vol. 10, No. 6, 2003, pp. 2586–2592.

[20]Lafleur, T., Charles, C., and Boswell, R., "Ion beam formation in a very low magnetic field expanding helicon discharge," *Physics of Plasmas*, Vol. 17, No. 4, 2010, pp. 043505.

[21]Lafleur, T., Charles, C., and Boswell, R., "Plasma control by modification of helicon wave propagation in low magnetic fields," *Physics of Plasmas*, Vol. 17, No. 7, 2010, pp. 073508.

[22]Lafleur, T., Charles, C., and Boswell, R., "Electron temperature characterization and power balance in a low magnetic field helicon mode," *Journal of Physics D: Applied Physics*, Vol. 44, No. 18, 2011, pp. 185204.

[23]Lafleur, T., Charles, C., and Boswell, R., "Characterization of a helicon plasma source in low diverging magnetic fields," *Journal of Physics D: Applied Physics*, Vol. 44, No. 5, 2011, pp. 055202.

[24]Little, J. M. and Choueiri, E. Y., "Critical condition for plasma confinement in the source of a magnetic nozzle flow," *IEEE Transactions on Plasma Science*, Vol. 43, No. 1, 2014, pp. 277–286.

[25]Little, J. and Choueiri, E. Y., "Electron cooling in a magnetically expanding plasma," *Physical review letters*, Vol. 117, No. 22, 2016, pp. 225003.

[26]West, M. D., Charles, C., and Boswell, R. W., "Operating radio frequency antennas immersed in vacuum: Implications for ground-testing plasma thrusters," *Journal of Propulsion and Power*, Vol. 26, No. 4, 2010, pp. 892–896.

[27]Andersen, S., Jensen, V. O., Nielsen, P., and D'Angelo, N., "Continuous supersonic plasma wind tunnel," *The Physics of Fluids*, Vol. 12, No. 3, 1969, pp. 557–560.

[28]Boswell, R. W., "Very efficient plasma generation by whistler waves near the lower hybrid frequency," *Plasma Physics and Controlled Fusion*, Vol. 26, No. 10, 1984, pp. 1147.

[29]Chen, F. F., "Plasma ionization by helicon waves," *Plasma Physics and Controlled Fusion*, Vol. 33, No. 4, 1991, pp. 339.

[30]Degeling, A., Jung, C., Boswell, R., and Ellingboe, A., "Plasma production from helicon waves," *Physics of Plasmas*, Vol. 3, No. 7, 1996, pp. 2788–2796.

[31]Shamrai, K. P. and Taranov, V. B., "Volume and surface rf power absorption in a helicon plasma source," *Plasma Sources Science and Technology*, Vol. 5, No. 3, 1996, pp. 474.

[32]Lorenz, B., Krämer, M., Selenin, V., and Aliev, Y. M., "Excitation of short-scale fluctuations by parametric decay of helicon waves into ion–sound and Trivelpiece–Gould waves," *Plasma Sources Science and Technology*, Vol. 14, No. 3, 2005, pp. 623.

[33]Merino, M. and Ahedo, E., "Influence of electron and ion thermodynamics on the magnetic nozzle plasma expansion," *IEEE Transactions on Plasma Science*, Vol. 43, No. 1, 2014, pp. 244–251.

[34]Chen, F. F., "Helicon discharges and sources: a review," *Plasma Sources Science and Technology*, Vol. 24, No. 1, 2015, pp. 014001.